

# Stretchable Electronic Facial Masks for Sonophoresis

Shuang Li, Jingwen Xu, Rui Li, Yongkang Wang, Maoyi Zhang, Jie Li, Shizhen Yin, Guodong Liu, Lijuan Zhang, Baoqiang Li, Qi Gu, and Yewang Su\*



Cite This: *ACS Nano* 2022, 16, 5961–5974



Read Online

ACCESS |



Metrics & More



Article Recommendations



Supporting Information

**ABSTRACT:** We introduce a stretchable electronic facial mask (SEFM) as a platform for facial healthcare, which can integrate with various sensors and actuators. As a demonstration, an SEFM for sonophoresis enabling the promotion of the delivery effect of a drug mask is developed. To overcome the technique challenges, several approaches including the design of the joined silicone layer by two planar half-face portions and the single-side soft pressing (SSSP) technique for encapsulation are exploited in this work, which could be extended to the design and fabrication of other stretchable electronics. The mechanical, thermal, electrical, and ultrasonic characteristics of the SEFM are all verified by the finite element analysis and experiments. Finally, we prove the effect of the SEFM on accelerating the delivery of hyaluronic acid (HA) through animal experiments and confirm that the SEFM can enhance the skin moisture content by 20% via human facial experiments.

**KEYWORDS:** flexible electronics, stretchable electronics, facial masks, sonophoresis, transdermal drug delivery



Transdermal drug delivery has made an important contribution in medical treatment for thousands of years.<sup>1</sup> The strategies for accelerating the delivery of drugs mainly include conventional chemical enhancers,<sup>2,3</sup> iontophoresis,<sup>4–7</sup> sonophoresis,<sup>8,9</sup> microneedles,<sup>10–12</sup> etc. Sonophoresis, in which ultrasound is used for the delivery of drugs into/through the skin, such as glycerin, hyaluronic acid (HA), nicotinamide, and nanoparticles,<sup>13–16</sup> dates back to as early as the 1950s.<sup>17</sup> Compared with conventional chemical enhancers and iontophoresis, sonophoresis can increase the skin permeability for a broader range of molecular weights up to tens of thousand Daltons (the length at nanoscale) without involving irritation or toxicity to living cells and serious skin pain.<sup>1</sup> Microneedles are broadly capable of delivering not only small molecules but also macromolecules; however, they are physically invasive, which raises additional considerations about safety and sterility.<sup>1</sup> Sonophoresis involves low-frequency sonophoresis (LFS, 20–100 kHz) and high-frequency sonophoresis (HFS,  $\geq 0.7$  MHz), both of which are mainly based on the cavitation effect, but the LFS acts on the skin surface, while the HFS takes effect in the skin.<sup>18</sup> Other mechanisms, such as the thermal effect, may also play nonnegligible roles in some cases.<sup>18–22</sup> For example, one of the earlier studies reported that low-frequency ultrasound can induce significant transdermal transport of proteins, including insulin ( $\sim 6$  kDa), interferon  $\gamma$  ( $\sim 17$  kDa), and erythropoietin ( $\sim 48$  kDa).<sup>23</sup> Another work showed that continuous ultra-

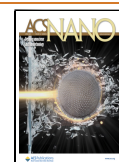
sound at 1 MHz and 400 mW/cm<sup>2</sup> can accelerate the absorption of HA of 1000 kDa and 3000 kDa in size.<sup>13</sup>

It is a promising idea to apply the technique of sonophoresis to human facial healthcare, since improving facial health conditions is of great significance for people of all ages.<sup>24–26</sup> A wearable electronic device can be developed based on the technique of sonophoresis for facial healthcare. The optimal strategy faces several requirements/challenges: (1) Perfect conformal fit: the propagation of ultrasound needs a medium, but the air between the ultrasonic emission probe and the skin greatly reduces the propagation efficiency, thus a perfect conformal fit between the probe and face skin is essential. (2) Hands-free for personal long-time use: the process of facial healthcare usually lasts tens of minutes, during which, it is preferable if the hands are free for other jobs at the same time. The existing hand-held ultrasound devices cannot meet this requirement.<sup>27,28</sup> (3) Large-area and complex surface of human faces: the first and the second conditions require that the developed wearable device has a conformal fit to the entire

**Received:** December 16, 2021

**Accepted:** March 29, 2022

**Published:** April 1, 2022



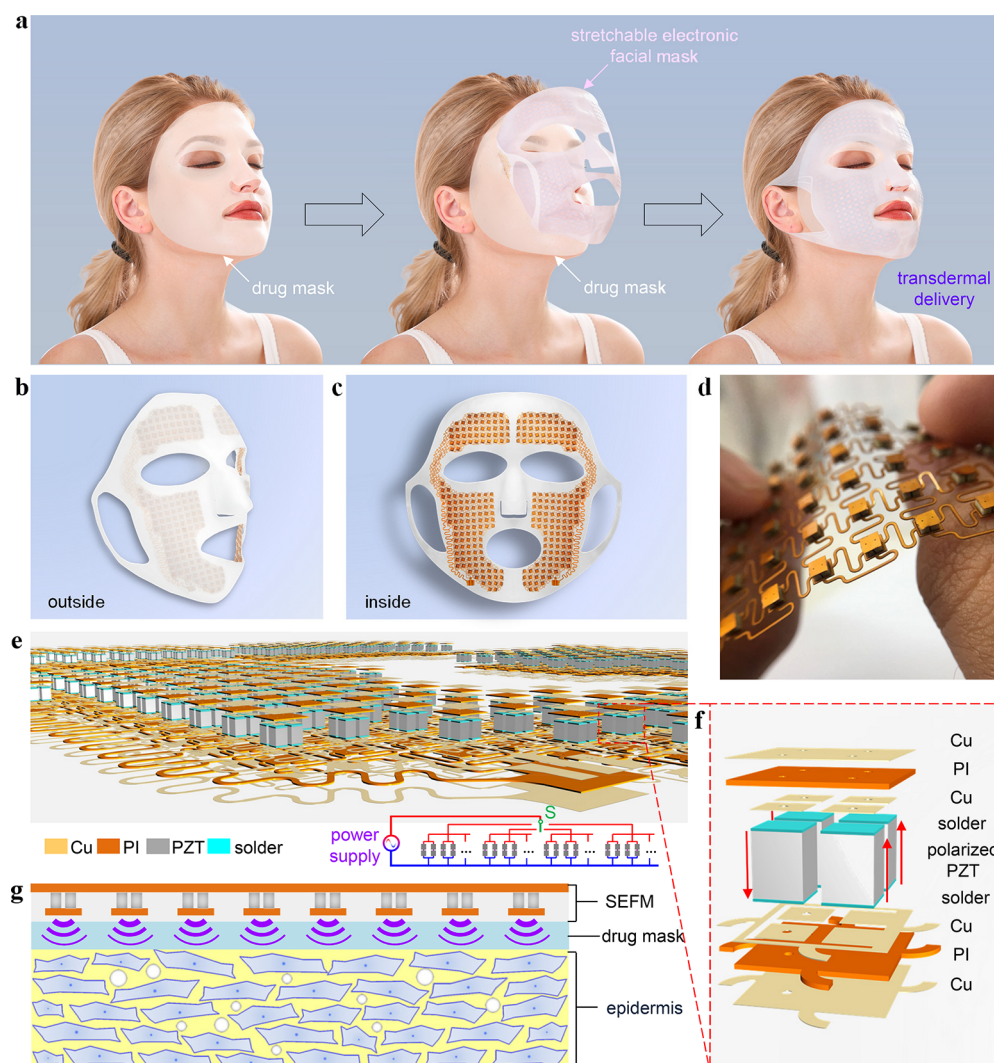


**Figure 1.** Display and mechanism of the SEFM. (a) Schematic illustration of the use of the SEFM. (b) Outside and (c) inside view of the SEFM. (d) Optical image of the stretchable island-bridge mesh circuit. (e) Layout of the stretchable island-bridge mesh circuit and its equivalent circuit diagram. (f) Enlarged view of an island taken from panel e. (g) Schematic illustration of the underlying mechanism of sonophoresis by the SEFM.

surface of the human face, which, however, is a large-area and complex undevelopable surface. Researchers have designed and prepared a series of flexible/stretchable ultrasonic devices in recent years,<sup>29–44</sup> which have great potential in medical treatment and healthcare applications. The majority of these flexible/stretchable ultrasonic devices were applied on complex surfaces for imaging/monitoring of the internal structure, such as three-dimensional images of complex defects,<sup>29</sup> central blood pressure,<sup>38</sup> deep-tissue hemodynamics,<sup>39</sup> and blood flow velocity.<sup>40</sup> In addition, the therapeutic capacity, such as accelerating chronic wound healing,<sup>35</sup> has also been studied recently based on such devices. On the other hand, the large-area and complex surface of human faces still brings huge technical challenges, and the function of sonophoresis has not been investigated in these flexible/stretchable devices.

Here, we introduce a concept of a stretchable electronic facial mask (SEFM), which satisfies the above three requirements simultaneously and can be used as a platform for human facial healthcare with various functions. Nano/microsensors for water content, elasticity and roughness; and actuators for photodynamics, ultrasonic, radio frequency, heating, etc. can

be integrated on the platform to achieve signal monitoring and active healthcare. As a device-level demonstration, functional components for sonophoresis (piezoelectric arrays) are integrated on the platform for the promotion of drug delivery. The SEFM for sonophoresis consists of a stretchable island-bridge mesh circuit, specially designed piezoelectric arrays with a resonant frequency of  $\sim 1$  MHz, and human-face-like encapsulation layers. To overcome the technique challenges and satisfy the requirements in applications, the design of single-side structure for the piezoelectric components, the design of a joined silicone layer by two planar half-face portions, the single-side soft pressing (SSSP) technique for the encapsulation, the design of an organic–inorganic composite structure, and the four-pillar design with a slender aspect are exploited in this work, which could be extended to the design and fabrication of other stretchable electronics. The mechanical, thermal, electrical, and ultrasonic characteristics of the SEFM are all verified by finite element analysis (FEA) and experiments. Furthermore, the effects of the SEFM on accelerating the delivery of HA and enhancing the skin moisture content are verified by animal skin experiments and

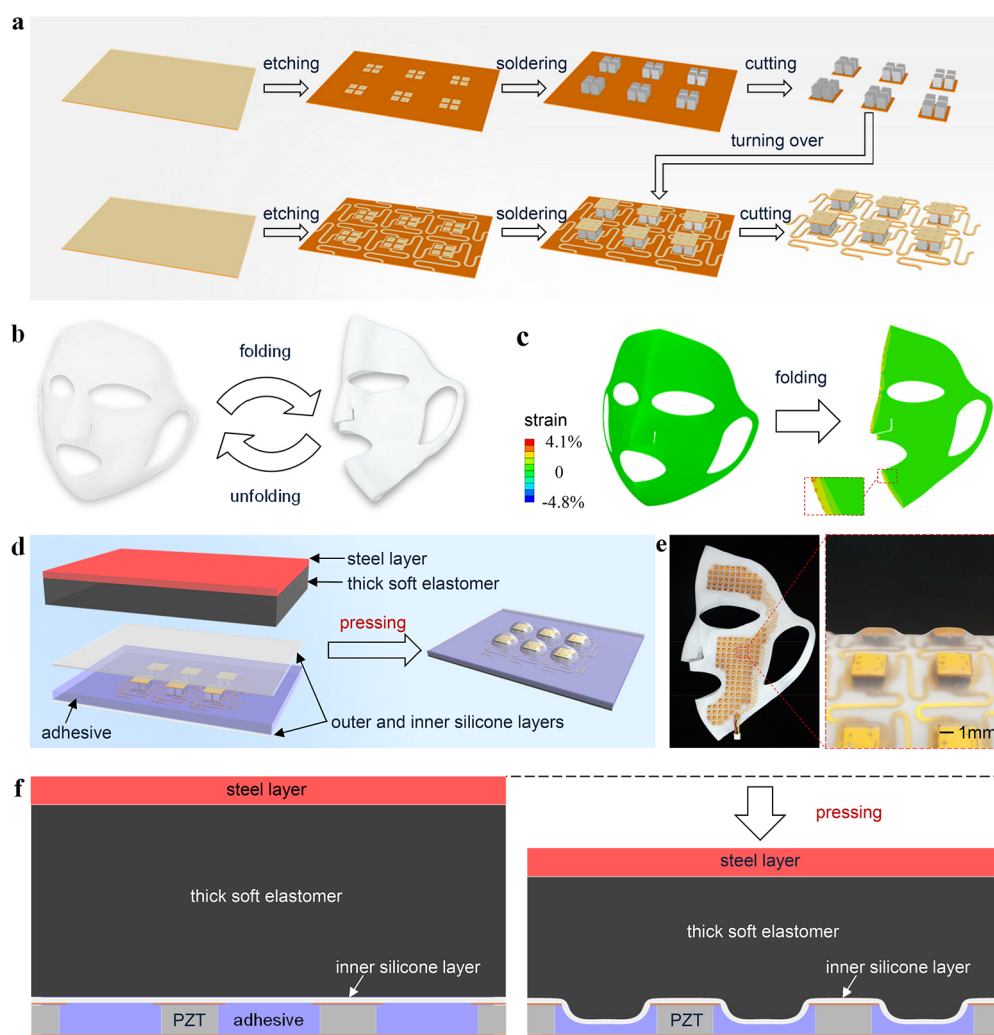


**Figure 2.** Design and fabrication of the SEFM. (a) Fabrication process of the stretchable island-bridge mesh circuit of the SEFM. (b) Folding/unfolding of the outer silicone layer for encapsulation. (c) FEA of the strain change between the two regimes of folding/unfolding. (d) The SSSP technique for the encapsulation. (e) Optical image of the SEFM and the enlarged uneven morphology of the inner surface after encapsulation. (f) The interaction among the thick soft elastomer, the island-bridge mesh structure, the adhesive, and the encapsulation layers.

human facial tests, respectively. Other drugs, which have been proven in previous literature, can also penetrate the skin more effectively by using the SEFM to achieve a different therapeutic efficacy. The comprehensive results of this study indicate tremendous potential of the developed SEFM for facial healthcare applications.

## RESULTS AND DISCUSSION

**Display and Mechanism of the SEFM.** Figure 1a shows the way to use the SEFM for sonophoresis, which is human-face-like and with ear hooks (Figure 1b,c). A drug mask consisting of water, glycerin, HA, nicotinamide, and other drugs is applied before wearing the SEFM. The flexibility, stretchability, and design of the curved surface and ear hooks ensure that the entire SEFM has a conformal fit to the drug mask and the human face. A developed controller consisting of circuits and a mobile battery is connected to the SEFM via an electronic wire for the programmatic ultrasonic excitation. The SEFM is a sandwich structure consisting of the stretchable island-bridge mesh circuit<sup>45–49</sup> integrated with piezoelectric arrays (Figure 1d) for ultrasonic excitation encapsulated by the

outer and inner stretchable silicone layers, which are white and transparent, respectively. Figure 1e and f depict the oblique view of the enlarged island-bridge mesh circuit and a piezoelectric component consisting of the multilayer configuration of Cu/PI/Cu/solder/polarized lead zirconate titanate (PZT)/solder/Cu/PI/Cu, respectively (details shown in Figures S1 and S2). On each island, the piezoelectric component is divided into four slender pillars so that a stable and pure vibration mode perpendicular to the skin results. The four polarized slender pillars can be divided into two groups. The two pillars in each group are connected in parallel (the same polarized direction) but have an opposite polarized direction from the other group. The two groups of slender pillars are connected in series so that the interconnections locate on only one side of the piezoelectric components. Figure 1g illustrates the underlying mechanism of sonophoresis by the SEFM. The cavitation effect of the ultrasound causes bubbles in the cavities among the corneocytes of the stratum corneum, and the oscillating cavitation bubbles induce disordering of the lipid bilayers of the stratum corneum, realizing the increase of skin permeability.<sup>18</sup> In addition, the thermal effect may also



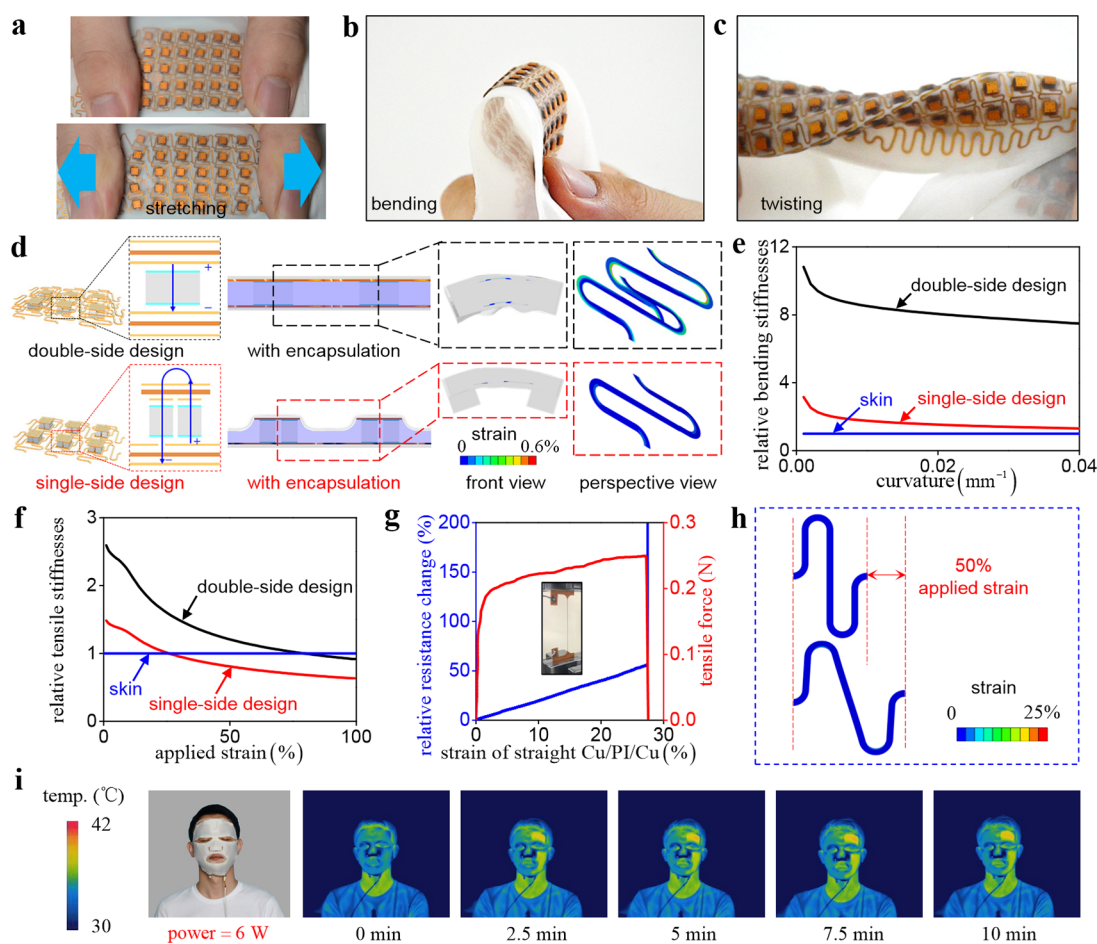


**Figure 3.** Mechanical and thermal performances of the SEFM. Large deformation of the SEFM: (a) stretching, (b) bending, and (c) twisting. (d) Comparison of the single-side and double-side designs as well as strain distribution in the two designs under a bending curvature of  $0.022 \text{ mm}^{-1}$ . (e) Relative bending stiffness to human skin versus the bending curvature. (f) Relative tensile stiffness to human skin versus the applied strain. (g) Tensile force and relative resistance change versus the applied strain of a straight  $18/100/18\text{-}\mu\text{m}$ -thick Cu/PI/Cu composite structure. (h) Strain distribution in the serpentine interconnect made of the Cu/PI/Cu composite structure when uniaxially stretched to 50% applied strain. (i) Temperature distribution in a half SEFM on the face with input of 6 W electric power under an ambient temperature of  $30^\circ\text{C}$ .

play additional roles by increasing the kinetic energy and diffusivity of drugs, dilating hair follicles and sweat glands, and enhancing the circulation of blood in the treated area.<sup>18</sup>

**Design and Fabrication of the SEFM.** The fabrication of the stretchable island-bridge mesh circuit of the SEFM is outlined in Figure 2a. First, photolithography and wet etching were applied to one side of a laminated film consisting of Cu/PI/Cu with a thickness of  $18 \mu\text{m}/100 \mu\text{m}/18 \mu\text{m}$ , respectively. Here, the design of a thick Cu layer is of great significance to reduce the thermal loss and ensure the electrical performance of the SEFM.<sup>49</sup> The thick PI layer is beneficial to increasing the ductility of Cu by delocalizing its deformation,<sup>50–52</sup> enhancing the restoring ability and antifatigue ability.<sup>53</sup> Through-hole punching and Cu deposition were used at certain locations of the etched film to connect electrodes of the two sides. A 1.3-mm-thick PZT plate was polarized and mechanically cut into  $1 \text{ mm} \times 1 \text{ mm} \times 1.3 \text{ mm}$  slender pillars. The prepared piezoelectric slender pillars were then soldered onto the designed location, as shown in the top subgraphs of Figure 2a. By laser cutting, the piezoelectric components were obtained. Second, another laminated film ( $18 \mu\text{m}/100 \mu\text{m}/18 \mu\text{m}$ -thick) was also prepared by the techniques of photolithography, wet etching, through-hole punching, and Cu deposition, but with a

different pattern, as shown in the bottom subgraphs of Figure 2a. The prepared piezoelectric components were then turned over and soldered onto the later prepared laminated film. The stretchable island-mesh circuit was finally obtained by laser cutting.

One key technique challenge is how to encapsulate a planar island-bridge mesh circuit into silicone layers with a complex undeveloped surface. The only experience from the literature is the prestrain strategy that the circuit is bonded onto the silicone layer after the silicone layer is stretched into a planar shape.<sup>54</sup> Release of the prestrain results in the encapsulated SEFM with a complex undeveloped face-like surface. However, this strategy is impractical here because the surface is very complex and is with irregular edges. Even though this strategy is applied, the geometric form of the encapsulated SEFM will be very unsmooth and ugly, because the silicone layer is too thin to force the island-bridge mesh structure within a smooth surface. Here, this challenge is overcome by the design of the joined silicone layer by two planar half-face portions. Considering the practical shape of human faces, the outer silicone layer for encapsulation is designed as in Figure 2b, which consists of two planar portions joined along a nonstraight edge for two half faces. The corresponding inner



encapsulation consists of two separated silicone layers with the half-face planar portion. The encapsulating operation can be conducted half face by half face, when the outer silicone layer is folded into the planar regime. Finite element analysis (FEA, Figure 2c) shows that the change of the maximum strain between the two regimes is quite small (4.1%) and occurs only at the region near the edges. For the region where the island-bridge mesh structure locates, the strain change approaches zero (details shown in Note S1, Supporting Information), which reduces the difficulties of the encapsulation operation. Wearing experience also confirms that the designed silicone layer is able to have a conformal fit to the entire surface of the human face without uncomfortable tension. Instead of a breathable material, silicone is used for the encapsulation of the SEFM, because the existing breathable materials commonly contain a pore structure<sup>55,56</sup> and are not suitable for the propagation of the ultrasound. In the future, a breathable material that does not significantly weaken the ultrasound could be developed for the encapsulation layer to optimize the comfort of the SEFM.

In order to maintain a low stiffness of the encapsulated SEFM, the optimal strategy is filling the adhesive between the outer and inner silicone layers as little as possible, although the island-bridge mesh structure has a bumpy morphology. As shown in Figure 2d, a single-side soft pressing (SSSP) technique for the encapsulation is exploited to accomplish the ideal regime (Figure 2e) that the inner transparent silicone layer deforms locally to fit the morphology of the island-bridge mesh structure, while the outer silicone layer keeps almost planar. As demonstrated in Figure 2d, the island-bridge mesh structure is sandwiched by the outer and inner silicone layers, with liquid adhesive (K-705, Kafuter, China) filling in between. The pressure is applied, via a composite plate consisting of a stiff steel layer (with Young's modulus of 210 GPa and thickness of 3 mm) and a thick soft elastomer (with a Young's modulus of 60 kPa and thickness of 12 mm), to the unfinished encapsulated SEFM and held until the liquid adhesive is completely solidified. Figure 2f illustrates the interaction among the thick, soft elastomer; the island-bridge mesh structure; the adhesive; and the encapsulation layers. The inner transparent silicone layer is locally forced into the spaces between adjacent islands by the pressure, via the thick soft elastomer. The excess adhesive is then forced out from the edge of the SEFM and cleaned up. The bumpy morphology holds at the inner surface of the encapsulated SEFM after complete solidification. The encapsulating operation for the SEFM can be conducted half face by half face (details shown in Figure S4). After the encapsulating operation, the weight of the SEFM is about 54.8 g. For a face area of about 20 cm × 20 cm, the pressure caused by the weight only (without consideration of the tension of the SEFM) can be estimated as 13.7 Pa, which would not result in users' discomfort.<sup>57,58</sup>

### Mechanical and Thermal Performances of the SEFM.

The fabricated SEFM for sonophoresis can withstand relatively large deformation such as stretching, bending, and twisting (Figure 3a–c), which enables it to have a conformal fit with the entire human face. The exceptional mechanical performance is mainly due to the design of a single-side structure (Figures 3d and S5), i.e., the interconnections locate at only one side of piezoelectric components, and the SSSP technique. The four polarized slender pillars can be divided into two groups. The two pillars in each group are connected in parallel by sharing the top and bottom Cu/PI/Cu laminated films but

have an opposite polarized direction with the other group. The two groups of slender pillars are connected in series by the top Cu/PI/Cu laminated film so that the interconnections locate at only one side of the piezoelectric components. An alternative design is the double-side structure (Figure 3d), which is simpler for the electronic connections. Figure 3d and Figure S5 show the difference between the two designs and the comparison of strain distribution of the two structures subject to the same bending curvature of 0.022 mm<sup>−1</sup> (details of the FEA shown in the Experimental Section). It was found that the maximum principal strain of the double-side structure is 0.6%, while that of the single-side structure is only 0.1%. The relative bending and tensile stiffnesses to the human skin (with Young's modulus of 600 kPa and thickness of 1.5 mm)<sup>59</sup> are studied in Figure 3e and f versus the bending curvature and applied strain, respectively (details shown in Note S2, Supporting Information). The bending curvature up to 0.04 mm<sup>−1</sup> corresponding to a radius of 2.5 cm and an applied strain up to 100% are enough for practical application (Figure S3). Here, the parts of the "island" have been considered in the definitions of the bending curvature and applied strain, as well as the computation of the bending and tensile stiffnesses. Both of the stiffnesses of the single-side structure, which are on the same order of magnitude as human skin, are much lower than those of the double-side structure, implying the superiority of the single-side design.

It has been revealed in Figure 1 that the present design involves the Cu/PI organic–inorganic composite structure, which, according to the literature,<sup>50–53</sup> helps increase the ductility of Cu by delocalizing its deformation. To validate the protective effect of PI against rupture of Cu, we conducted a uniaxial tensile test for a straight Cu/PI/Cu composite structure with thicknesses of 18 μm, 100 μm, and 18 μm; a length of 40 mm; and a width of 0.3 mm. The curves of tensile force and relative resistance change versus the applied strain in Figure 3g show that the failure strain of the composite structure (>25%) is much larger than that of a single layer of Cu (~1.5%), thus the former can provide robust stretchability. The FEA in Figure 3h suggests that the maximum strain of the serpentine interconnection made of the Cu/PI/Cu composite structure in the SEFM is far below its ductility even when uniaxially stretched to an applied strain as large as 50%, confirming the safety under large deformation. To verify its durability and stability, a rectangular sample with an area of 4 cm × 4 cm was fabricated and tested via 2000 tension-releasing cycles of 20% applied strain and 3.2 mm/s velocity. Due to the viscoelastic property of the silicone layer, the tensile force is slightly reduced by 10% after 2000 cycles (Figure S6a,b). Figure S6c shows that the solidified adhesive (K-705, Kafuter, China) was not dislocated basically after 2000 cycles because of its strong adhesion and good elasticity, while only small local interfacial separations occur at some edges of the islands (indicated by the red arrows). It should be noted that, by adopting physical vapor deposition processes, the stretchability of the SEFM can be further improved.<sup>40,47,51</sup> In this work, photolithography and wet etching of laminated films were adopted to reduce the process cost of the stretchable mesh circuits, considering that such laminated films can be obtained from the market economically.

Two demands are required to achieve a high energy conversion efficiency. One is the good impedance matching between the SEFM and the controller,<sup>60,61</sup> which has been accomplished by the optimal design of the circuit of the

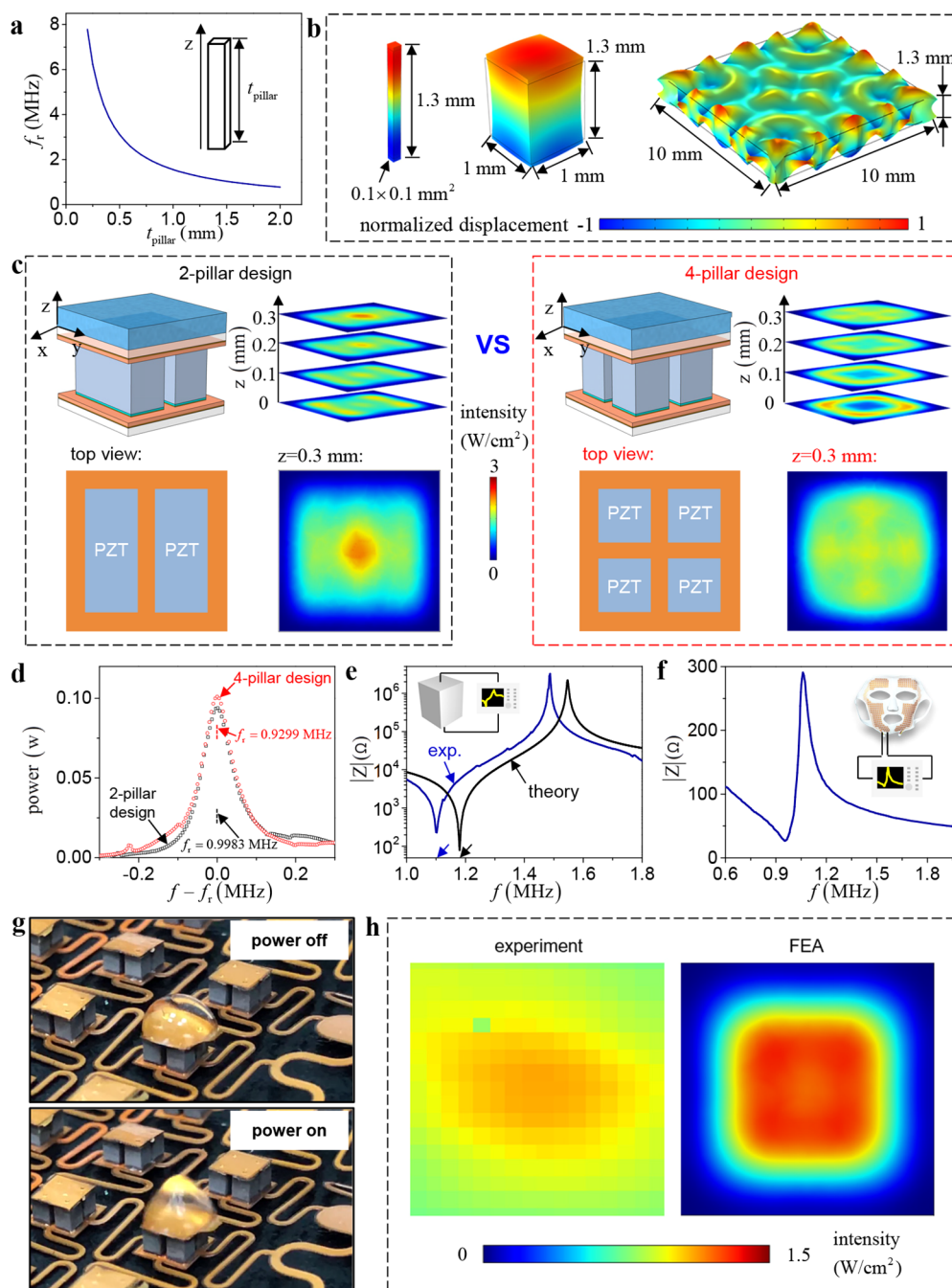


**Figure 4.** Design and performances of the piezoelectric component. (a) Relationship between the resonant frequency and the thickness of a piezoelectric pillar obtained by a one-dimensional piezoelectric theoretical model. (b) Comparison of vibration modes of the piezoelectric pillars with different cross-sectional areas. (c) Comparison of sound intensity distribution between the two-pillar and four-pillar designs. (d) Comparison of total power of sound field between the two-pillar and four-pillar designs. (e) Impedance–frequency curve of a single  $1.0 \times 1.0 \times 1.3 \text{ mm}^3$  piezoelectric pillar. (f) Impedance–frequency curve of a quarter of the final SEFM. (g) The visual effect of the SEFM that emits ultrasound to a water drop. (h) Comparison of sound field distribution between the experiment and the FEA at a depth of 8 mm.

controller according to the impedance characteristics of the SEFM. Another is to reduce the resistance of the serpentine interconnections as much as possible, because a large resistance yields useless thermal loss. It is verified that the resistance of the thick serpentine interconnection is only  $37.54 \text{ m}\Omega$  (details shown in the [Experimental Section](#)) and the contact resistance between the piezoelectric component and the island-bridge mesh structure is also on the order of milliohms, which are both far below the impedance of the piezoelectric component ( $\sim 200 \Omega$ ), thus the electrical energy

of the SEFM is mainly converted into ultrasonic energy emitted by the piezoelectric components rather than thermal energy of the serpentine interconnections. [Figure 3i](#) demonstrates the temperature distribution (FLIR T420, FLIR Systems, USA) in a half SEFM on the face with an input of  $6 \text{ W}$  of electric power under an ambient temperature of  $30^\circ\text{C}$ , considering that the SEFM may be used in summer. It is observed that the maximum temperature in the device is maintained at  $42^\circ\text{C}$  after  $5 \text{ min}$ , which is less than the threshold temperature of about  $43^\circ\text{C}$  provided by a previous

study,<sup>62</sup> reflecting no serious thermal comfort problems when applying the SEFM.

**Design and Performances of the Piezoelectric Component.** The parameter design of the piezoelectric component is of much importance for the realization of its function. We first studied the one-dimensional theoretical model for a piezoelectric pillar, which shows that the resonant frequency  $f_r$  and the thickness  $t_{\text{pillar}}$  of the pillar satisfy the equation

$$\frac{d_{33}^2}{l_{33}^T s_{33}^E} \tan\left(\frac{\pi f_r}{c} t_{\text{pillar}}\right) = \frac{\pi f_r}{c} t_{\text{pillar}} \quad (1)$$

where  $d_{33}$ ,  $l_{33}^T$ ,  $s_{33}^E$ , and  $c$  are the piezoelectric strain constant, the dielectric constant, the elastic constant, and the wave velocity in the  $z$  direction, respectively (Note S3, Supporting Information). For  $d_{33} = 2.9 \times 10^{10}$  C/N,  $l_{33}^T = 5.69 \times 10^{-9}$  C<sup>2</sup>/(N × m<sup>2</sup>),  $s_{33}^E = 1.56 \times 10^{-11}$  Pa<sup>-1</sup>, and  $c = 3900$  m/s, Figure 4a gives the relationship between the resonant frequency  $f_r$  and the thickness  $t_{\text{pillar}}$ . According to a large number of previous studies,<sup>18</sup> the frequency of 1 MHz has been proved to be effective for sonophoresis. Therefore, the 1 MHz piezoelectric component is preferred for the SEFM. The thickness  $t_{\text{pillar}}$  of the piezoelectric pillar is chosen as 1.3 mm, because its resonant frequency is slightly higher than the target of 1 MHz for sonophoresis (Figure S9a) such that ~1 MHz is achieved after the subsequent integration. Optimal design of the frequency can be carried out in the future. The vibration mode of the piezoelectric pillar with a constant thickness changes with the cross-sectional area under a given one-dimensional resonant frequency excitation. For example, the vibration modes (FEA, details shown in the Experimental Section) of the piezoelectric pillars with  $0.1 \times 0.1$  mm<sup>2</sup> and  $1.0 \times 1.0$  mm<sup>2</sup> cross sections are close to one-dimensional longitudinal vibration, while the vibration mode for the  $10 \times 10$  mm<sup>2</sup> case is irregular (Figure 4b). For easy preparation, the cross section of  $\sim 1.0 \times 1.0$  mm<sup>2</sup> is preferred.

As shown in Figure 4c, we also compared the sound intensity distributions of the two-pillar and four-pillar designs, with cross sections of  $1.0 \times 2.35$  mm<sup>2</sup> and  $1.0 \times 1.0$  mm<sup>2</sup> for each pillar, respectively (details shown in the Experimental Section). When an excitation voltage  $f = f_r$  with an amplitude of 22.5 V is applied to each piezoelectric pillar, the sound intensity distribution of the four-pillar design is more uniform than that of the two-pillar design, and the total power of sound field of the former at  $z = 0.3$  mm and  $z = 0.2$  mm in water is larger than that of the two-pillar design, with a difference of ~10% (Figure 4d and Figure S9b). The total power of the four-pillar design near the resonant frequency maintains 80% of the peak value even if the frequency deviation is  $\pm 20$  kHz, implying the robustness of the performances of the piezoelectric component. Comparison of the average vibration displacement amplitudes between the two-pillar and four-pillar designs is shown in Figure S9c. Therefore, we finally prefer the four-pillar design with  $1.0 \times 1.0 \times 1.3$  mm<sup>3</sup> piezoelectric pillar. It is worth noting that the peak value of sound intensity under the present working conditions is less than 3 W/cm<sup>2</sup>, which is safe according to the previous literature.<sup>18</sup> The island-bridge mesh circuit of the SEFM mainly consists of the serpentine interconnections and the piezoelectric components, which dominate the stretchability and the ultrasonic performance, respectively. It is a challenge to simultaneously achieve the high stretchability and ultrasonic performance for the SEFM,

which could be overcome by the following two strategies: (1) optimizing the stretchability of the serpentine interconnections by cross-section design and geometric configuration design and higher-precision patterning technology,<sup>47</sup> so that the area proportion of piezoelectric components can be enlarged while the apparent stretchability holds; (2) scaling down the in-plane sizes of the piezoelectric component and the serpentine interconnection in the same proportion, so that the homogeneity of the ultrasonic performance is enhanced.

Before fabricating the SEFM, we experimentally tested the resonance performance of a single piezoelectric pillar. The tested curve of the impedance  $|Z|$  versus the frequency of the piezoelectric pillar, which gives the resonant frequency as 1.1 MHz (Figure 4e), is close to that from the one-dimensional theory (Note S3, Supporting Information). The impedance–frequency curves of piezoelectric pillars with the same cross-sectional area ( $1.0$  mm  $\times$   $1.0$  mm) and different thickness (0.7, 1.0, 1.7, and 2.0 mm) were also tested, as shown in Figure S10. The one-dimensional theory can successfully estimate the resonant frequency when the thickness is more than 1.0 mm. For a thickness of 0.7 mm or less with a cross-sectional area of  $1.0$  mm  $\times$   $1.0$  mm, it could not be called a “pillar”. The vibration mode becomes more complex, and thus the one-dimensional theory is no longer effective. The same test was then applied to a quarter of the final encapsulated SEFM for the optimal design of the circuit of the controller to achieve impedance matching (Figure 4f).<sup>60,61</sup> The result shows that the resonant frequency is slightly decreased to about 1 MHz, thus the frequency of the output electrical signal of the excitation circuit needs to be set at 1 MHz. In addition, it is verified that the impedance–frequency curve of the SEFM is stable before and after 2000 tension-releasing cycles of 20% applied strain (Figure S6d, details shown in Note S4). To verify the device yield and uniformity of the SEFM before and after stretching, five rectangular samples with an area of  $4$  cm  $\times$   $4$  cm were fabricated and were tested before and after 1000 tension-releasing cycles of 20% applied strain. As shown in Figure S11, the impedance–frequency curves of the five samples basically coincide, especially at a resonant frequency of ~1 MHz, which demonstrates high device yield (100% for five samples) and high uniformity of the SEFM before and after stretching. In the application of the SEFM, the excitation voltage that has arisen from the designed controller is a sine wave with an amplitude of 45 V, a frequency of 1 MHz (continuous wave), and a duty cycle of 100%. To avoid a hyperthermia problem of the human face, the SEFM was divided into four portions with independent circuit channels (Figure S1), each of which works for only 5 s in a 20-s cycle.

The visual effect of the SEFM that emits ultrasound to a water drop is exhibited in Figure 4g and Video S1. For the power-off state, the entire water drop remains hemispherical, while it becomes tapered and jumps repeatedly for the power-on state. The visual effect that the SEFM emits ultrasound to  $3 \times 3$  water drops demonstrates the uniformity of the ultrasonic performance of each piezoelectric component (Figure S12 and Video S2). In order to confirm that the SEFM indeed emits ultrasound with an intensity magnitude of a watts per square-centimeter level, the sound intensity distribution was experimentally measured by using Ultrasound Test Tank systems (Precision Acoustics Ltd., UK; Figure S13). The sound field at a depth of 8 mm was measured and compared with the FEA result (Figure 4h). The maximum value of the



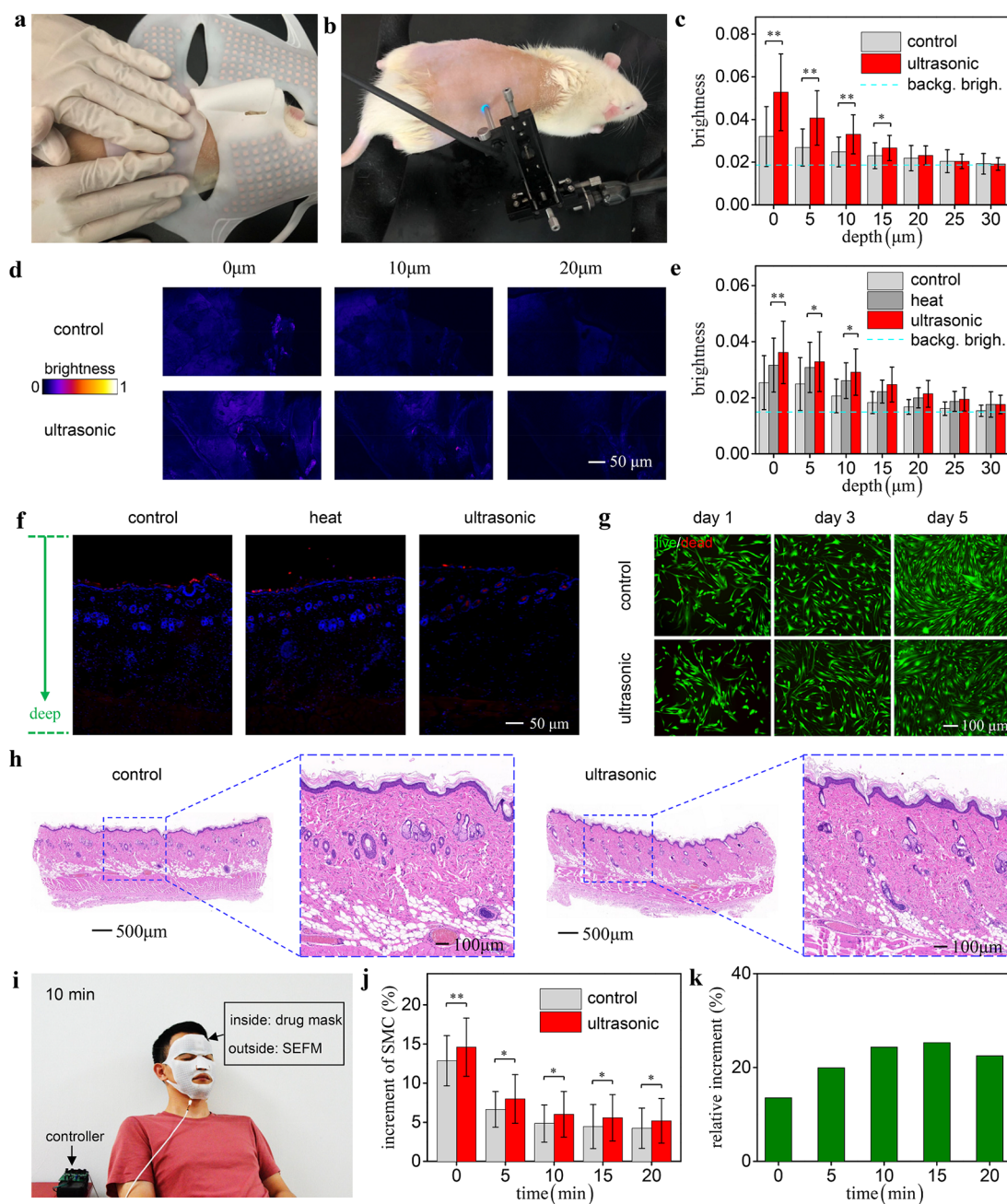


**Figure 5.** Transdermal delivery of HA by the SEFM. (a) Transdermal delivery of HA by the SEFM conducted on Sprague–Dawley rats. (b) Measurement of the rhodamine-labeled HA at different skin depths. (c) Comparison of the fluorescence brightness with different skin depths between the control group (32 samples) and ultrasonic group (32 samples). Every four samples were from the same rat in each group. The error bars represent the standard deviation. \*\* and \* represent  $P < 0.001$  and  $0.001 < P < 0.05$ , indicating significant differences between the control group and ultrasonic group. (d) Typical pseudocolor confocal micrographs at different skin depths of the both groups after pseudocolor processing. (e) Comparison of the fluorescence brightness with different skin depths among the control group (16 samples), heat group (24 samples), and ultrasonic group (24 samples). Every four samples were from the same rat in the heat group and the ultrasonic group, and every eight samples were from the same rat in the control group. The light blue dash represents the background brightness ( $\sim 0.0149$ ). The error bars represent the standard deviation. \*\* and \* represent  $P < 0.001$  and  $0.001 < P < 0.05$ , indicating significant differences between the heat group and ultrasonic group. (f) Comparison of tissue sections among the control group, heat group, and ultrasonic group showing the delivery of HA. (g) The results of live/dead staining about human dermal fibroblasts cocultured with SEFM ( $n = 3$ ). (h) Comparison of tissue sections between the control group and ultrasonic group showing the integrity of the epidermis and dermis. (i) Transdermal delivery of HA by the SEFM on the human face. (j) Comparison of the time-dependent increment of skin moisture content between the control group (50 samples) and ultrasonic group (50 samples). Every 10 samples were from the same volunteer but a different 10 days in each group. The error bars represent the standard deviation. \*\* and \* represent  $P < 0.001$  and  $0.001 < P < 0.05$ , indicating significant differences between the control group and ultrasonic group. (k) Relative increment of the mean value of the skin moisture content between the ultrasonic group and the control group.

measured sound intensity is found to be  $1.134 \text{ W/cm}^2$ , which reaches 76% of the maximum value of the FEA result.

**Transdermal Delivery of HA by the SEFM.** HA is accepted as an excellent moisturizing ingredient and thus is widely used in facial healthcare.<sup>63,64</sup> In order to verify the promotion effect of the SEFM on transdermal delivery of HA, a contrast experiment was conducted on the animal model of eight Sprague–Dawley rats (64 samples). The 1% rhodamine-labeled HA (5 kDa, the length on the order of 1 nm) was infiltrated with cloth and placed on the dorsum skin of the rats, which the SEFM was then placed upon and fit conformally. A quarter of the SEFM in the ultrasonic group (on one side of the dorsum) was applied by the excitation voltage of 1 MHz (6 W, 10 min), while the quarter in the control group (on another side of the dorsum) was without any excitation voltage (Figure 5a). When the control group and the ultrasonic group are compared, it can be found that all of the effects (such as reducing water evaporation by the silicone layer) except ultrasonic and thermal effects caused by the SEFM are excluded. After the transdermal delivery, the rhodamine-labeled HA at different skin depths was detected by an endoscopic confocal microscope (ViewnVivo, OptiScan, Australia; wavelength: 550–575 nm; four places from each side of the dorsum for detection), as shown in Figure 5b. More details are shown in the Experimental Section. The MATLAB program package is used to calculate the brightness of the confocal micrographs at different skin depths of the control group and the ultrasonic group. As shown in Figure 5c, the average brightness of the confocal micrographs from the ultrasonic group at different depths (0–15  $\mu\text{m}$ ) is significantly higher than that of the control group after 10 min, which indicates that the SEFM can substantially enhance the transdermal delivery of HA. The student *t* test was performed for the control group and the ultrasonic group, of which the statistical results are given in Table S2. According to the statistical results, the value “*t*” is much greater than “1” ( $t \gg 1$ ) and the value “*P*” is less than “0.05” ( $P < 0.05$ ) at different depths (0–15  $\mu\text{m}$ ), which indicates that the data from the transdermal delivery experiments are statistically significant at different depths (0–15  $\mu\text{m}$ ). The data at depths of 20–30  $\mu\text{m}$  do not show a significant difference ( $P > 0.05$ ), where the brightness is close to the background brightness. Details of the statistical analysis are shown in the Experimental Section. Here, the light blue dash represents the background brightness ( $\sim 0.0184$ ), that is, the brightness of the confocal micrographs when there is no drug delivery. Figure 5d provides typical confocal micrographs at different skin depths of both groups after pseudocolor processing (more confocal micrographs shown in Figure S14). The ultrasound has different promoting effects for various drugs with different chemical formulas and molecular weights.<sup>18</sup> According to our investigation, although the molecular weights of HA for sonophoresis in previous studies are not the same as that of our experiment, there are relevant examples for reference: for HA with a molecular weight of 3000 kDa, a commercial ultrasonic device (frequency, 1 MHz; sound intensity,  $400 \text{ mW/cm}^2$ ) improves the delivery depth by 270% after a three-day treatment;<sup>13</sup> for HA with a molecular weight of 600–1100 kDa, a commercial ultrasonic device (frequency, 1 MHz; pressure amplitude, 100 kPa) improves the delivery concentration by 50% after 10 min treatment.<sup>65</sup> Here, by the SEFM, the delivery concentration of HA can also be improved to 50% (at depth of 5  $\mu\text{m}$  in Figure

5c) after 10 min of treatment, which further confirms its effectiveness.

To verify the durability of the SEFM, the rectangular sample with an area of  $4 \text{ cm} \times 4 \text{ cm}$  is used for another contrast experiment on the animal model of another eight Sprague–Dawley rats. The promotion effect on transdermal delivery of HA after 2000 tension-releasing cycles was tested (ultrasonic group). In addition, the heat group (42  $^{\circ}\text{C}$ , controlled by a commercial programmable film-like heater, as shown in Figure S15) is added to clarify whether the mechanism of the SEFM is based on the thermal effect. The total sample size is 64, including 24 ultrasonic group data, 24 heat group data, and 16 control group data. Figure 5e shows that, after 2000 tension-releasing cycles, the SEFM still works well in promoting the transdermal delivery of HA, which is better than the control group and heat group. In addition to the cavitation effect, the thermal effect also plays a nonnegligible role in the transdermal delivery of HA. The student *t* test was performed for the heat group and the ultrasonic group, of which the statistical results are given in Table S3 (details of the statistical analysis shown in the Experimental Section). According to the statistical results, the value “*t*” is much greater than “1” ( $t \gg 1$ ) and the value “*P*” is less than “0.05” ( $P < 0.05$ ) at different depths (0–10  $\mu\text{m}$ ), indicating statistically significant differences between the heat group and ultrasonic group at different depths (0–10  $\mu\text{m}$ ). The data at depths of 15–30  $\mu\text{m}$  do not show a significant difference ( $P > 0.05$ ), where the brightness is close to the background brightness. This test proves that the underlying mechanism of the SEFM is not only a thermal effect.

Since the above measuring method is not intuitive enough, the delivery of HA of the three groups was observed by cutting skins into slices, as shown in Figure 5f. The rhodamine-labeled HA (red) was delivered more deeply in the ultrasonic group than those of the control group and heat group. It should be noted that the observation by the former measuring method is effective within a depth of only 30  $\mu\text{m}$ , while the brightness decreases to the level of background brightness and thus cannot be distinguished for a depth  $> 30 \mu\text{m}$ . The present method has a wider observation range, which shows that the rhodamine-labeled HAs are mainly distributed within 100  $\mu\text{m}$  (Figure 5f), and a small amount of HA has even penetrated through the whole skin. Both methods have advantages: the former is more convenient and real-time in processing data, while the latter has a wider observation range and the results are more intuitive.

The biocompatibility of SEFM on fibroblasts was investigated, as shown in Figure 5g and Figure S16. The cellular cytotoxicity was performed using a live/dead assay and CCK-8 assay after 1, 3, and 5 days of cocultivation with SEFM. The results indicated that fibroblasts were basically alive, and the number of dead cells was small during the 1–5 day shaping period (Figure 5g). Moreover, as the CCK-8 assay certified, the growth of cells of the SEFM group had no significant difference at all time points compared with the control group (Figure S16). Overall, these results showed that the SEFM had excellent biocompatibility with fibroblasts. In order to further detect whether the ultrasonic treatment causes skin injury, the skins of two sides of the dorsum from the control group and the ultrasonic group, respectively, were selected, fixed with 4% paraformaldehyde (PFA), embedded with paraffin, cut into slices with a thickness of 9  $\mu\text{m}$ , and observed by hematoxylin-eosin staining (Figure 5h). The results demonstrate that the



integrity of the epidermis and dermis was maintained in the ultrasonic treated rat skin. This experiment illustrates the effectiveness and the safety of the SEFM on the transdermal delivery of HA.

After the animal experiment, we indirectly detected the effect of the SEFM on the transdermal delivery of HA by measuring the moisture content in the human face skin, with the experimental setup shown in Figure 5i. Before the transdermal delivery, the skin moisture content of two sides of the human face was measured. A commercial drug mask consisting of HA and water was placed on the human face, which the SEFM was then placed on and fit in conformally. A quarter of the SEFM in the ultrasonic group (on one side of the human face) was applied by an excitation voltage of 1 MHz (6 W, 10 min), while the quarter in the control group (on another side of the human face) was without any excitation voltage. After the transdermal delivery, the residual water from the commercial drug mask on the human face was cleaned with a paper towel, and then the skin moisture content of the human face of both the control group and ultrasonic group was measured every 5 min by a commercial tester (FC1501, Szkie, China; Figure S17). Five volunteers participated in the facial experiment for 10 days, and each volunteer performed the above experimental process once a day. Although the large amplitude of the error bar in Figure 5j shows the difference of each volunteer's facial skin, the average value of 50 samples shows obvious regularity. The increments of skin moisture content (compared with the first measurement) of the ultrasonic group at different time after transdermal delivery are all higher than those of the control group (Figure 5j). The student *t* test was performed for the control group and the ultrasonic group, of which the statistical results are given in Table S4. According to the statistical results, the value "*t*" is much greater than "1" ( $t \gg 1$ ) and the value "*P*" is less than "0.05" ( $P < 0.05$ ), which indicates that the data from the experiments of enhancing the skin moisture content are statistically significant. Details of the statistical analysis are shown in the Experimental Section. The relative increment of the mean value of the skin moisture content between the ultrasonic group and the control group reaches as much as 20% (Figure 5k). Since HA is an excellent moisturizing ingredient, it can be inferred that the additional increase of skin moisture content in the ultrasonic group was caused by the delivery of more HA. In addition to the delivery of HA, the delivery of two other drugs commonly used in facial healthcare<sup>66,67</sup> (2% beta-glucan, 100 kDa; 2% d-panthenol, 205.25 Da) was carried out on the animal model of another six Sprague–Dawley rats by using the rectangular sample of the SEFM with an area of 4 cm × 4 cm. The operation process of the delivery is the same as that of the delivery of HA. The delivery of the two drugs in the control group and ultrasonic group was observed by cutting skins into slices, as shown in Figure S18. The two fluorescein sodium labeled drugs (green) are both delivered more deeply in the ultrasonic group than those of the control group, which demonstrates the effect of the SEFM on accelerating the transdermal drug delivery again.

## CONCLUSIONS

In summary, an SEFM is present as a platform for facial healthcare, which can integrate with various sensors and actuators. As a device-level demonstration, functional components for sonophoresis are integrated on the platform for the promotion of transdermal drug delivery. The SEFM

consists of a stretchable island-bridge mesh circuit, specially designed piezoelectric arrays with a resonant frequency of ~1 MHz, and face-like encapsulation. Key designs and techniques developed in this work include (1) the design of a single-side structure for the piezoelectric components to achieve the low bending stiffness and high bendability, (2) the joined silicone layer by two planar half-face portions enabling the encapsulation of the planar island-bridge mesh circuit and conformal fitting the human face, (3) the SSSP technique for the encapsulation process to maintain a low stiffness of the SEFM, (4) the organic–inorganic composite structure to enhance the ductility and the robustness of the bridge interconnections, and (5) the four-pillar design with a slender aspect for uniform sound intensity and large total power of the sound field, many of which could be extended to the design and fabrication of other stretchable electronics. The mechanical, thermal, piezoelectric, and ultrasonic characteristics of the components or the entire SEFM are verified by the FEA and experiments. Finally, animal skin experiments verify the effect of the SEFM on accelerating the delivery of HA by detecting the rhodamine-labeled HA at different skin depths using an endoscopic confocal microscope. Human facial experiments confirm that the SEFM can enhance the skin moisture content by 20%, which indirectly validated the effect on accelerating the delivery of HA again. The comprehensive results of this study indicate the tremendous potential of the developed SEFM for facial healthcare applications.

## EXPERIMENTAL SECTION

**FEA of the Resistance of Serpentine Interconnect.** To validate the electrical property of the serpentine interconnection, the FEA, by using the commercial software COMSOL, was conducted (Figure S7a). The steady-state modeling was carried out by choosing a physical field: "Electric Currents" in the "AC/DC" module. The electrical boundary conditions were defined such that one end of the serpentine interconnection was grounded and another end acted as a terminal to give a current of 1 A. The conductivity of copper was set to  $5.71 \times 10^7$  S/m. The resistance of the serpentine interconnection was obtained by dividing the electric potential in the terminal by a current of 1 A.

**FEA of the Deformation of Island-Bridge Structure with Encapsulation.** The FEA of the deformation of the island-bridge structure with encapsulation was conducted by using the commercial software ABAQUS. The compliant encapsulation, including the adhesive ( $C_{10} = 0.00805369$ ,  $C_{01} = 0.00201342$ , and  $D_1 = 2$ ) and the silicone layers ( $C_{10} = 0.134228$ ,  $C_{01} = 0.033557$ , and  $D_1 = 0.12$ ), was treated as a hyper-elastic material that was described by the Mooney–Rivlin model. PI was treated as a linear elastic material, with a Young's modulus of 2.5 GPa and a Poisson's ratio of 0.34. Cu was regarded as an ideal elastic plastic material, with a Young's modulus of 124 GPa, a Poisson's ratio of 0.33, and a yield stress of 372 MPa, corresponding to the elastic strain range of 0.3% (Figure S7b). The parts of the "island" were treated as rigid bodies, since their stiffnesses are much greater than those of the "bridge". The hexahedron element C3D8RH was adopted for the substrates, and the shell element S4R was adopted for PI and Cu.

**FEA of Vibration Modes of the Piezoelectric Pillar.** To compare the vibration modes of the piezoelectric pillars with different cross-sectional areas, the FEA was conducted using the COMSOL software. The frequency-domain modeling was carried out by choosing the physical fields of "Solid Mechanics" and "Electrostatics". The material parameters of PZT are shown in Note S5, Supporting Information. All of the solid mechanical boundary conditions were stress free. The ground voltage on the bottom surface of PZT was zero, and an alternating voltage with an amplitude of 22.5 V and a frequency of 1.179 MHz (one-dimensional resonant frequency) was applied on the top surface of PZT.



**FEA of Sound Field for the Encapsulated SEFM.** To compare the sound field generated by the two-pillar and four-pillar designs, the FEA was conducted in COMSOL software (geometric model and meshes shown in Note S6). The frequency-domain modeling was carried out by choosing the following three physical fields: "Pressure Acoustics, Frequency Domain", "Solid Mechanics", and "Electrostatics". The physics field of "Pressure Acoustics, Frequency Domain" was imposed on the layers of water, silicone, Cu (not directly contacting with the solder), and PI at the top and bottom. The physics field of "Solid Mechanics" was imposed on the layers of solder (60Sn-40Pb), Cu (directly contacting with the solder), and PZT in the middle. The physics field of "Electrostatics" was also imposed on the layer of PZT in the middle. PZT was set as a piezoelectric material, and the others were treated as linear elastic materials. The relevant material parameters are shown in Note S5, Supporting Information. All of the solid mechanical boundary conditions were stress free, and the outer boundaries of the physics field "Pressure Acoustics, Frequency Domain" were set as perfectly matched layers to absorb sound waves. The ground voltage on the bottom surface of PZT was zero, and an alternating voltage with an amplitude of 22.5 V was applied on the top surface of PZT.

**Transdermal Delivery of Rhodamine-Labeled HA.** Sprague–Dawley rats (males) (7 to 8 weeks old) were used as animal models. First, the rats were anesthetized with 1.5% lidocaine, then the back skin was scraped carefully. The 1% rhodamine-labeled HA (5 kDa) was infiltrated with cloth and placed on the dorsum skin of rats, and then the SEFM was placed on it. After treatments of 10 min, the rhodamine-labeled HA at different skin depths was detected by using the endoscopic confocal microscope (ViewnVivo, OptiScan, Australia; wavelength, 550–575 nm). The results in Figure 3i prove that, when one side of the SEFM works, the temperature on the other side does not rise. Since the animal experiment needs a control group without any physical effect, this verification is necessary. For the experiment in Figure 5c, eight Sprague–Dawley rats were used. Each rat provided eight samples, with four samples on one side of the dorsum for the control group and four samples on another side of the dorsum for the ultrasonic group. For the experiment in Figure 5e, the other eight Sprague–Dawley rats were used. For rats 1–6, each rat provided eight samples, with four samples on one side of the dorsum for the heat group and four samples on another side of the dorsum for the ultrasonic group. For rats 7 and 8, each rat provided eight samples for the control group.

**Statistical Analysis.** Student's *t* test was applied to certify the validity of the experimental data in transdermal delivery of HA. The quantitative values of the brightness of the confocal micrographs were selected as the analysis objects. For Figure 5c, the total sample size "*n*" is 64, including 32 ultrasonic group data and 32 control group data. The two-tailed testing method (degree-of-freedom = 31) was used to assess a significant difference of the data with the software SPSS Statistics. The statistical results are given in Table S2. According to the statistical results, the value "*t*" is much greater than "1" ( $t \gg 1$ ) and the value "*P*" is less than "0.05" ( $P < 0.05$ ) at different depths (0–15  $\mu\text{m}$ ), which indicates that the data from the transdermal delivery experiments are statistically significant at different depths (0–15  $\mu\text{m}$ ). The data at depths of 20–30  $\mu\text{m}$  do not show a significant difference ( $P > 0.05$ ), where the brightness is close to the background brightness. For Figure 5e, the sample size "*n*" for student's *t* test is 48, including 24 heat group data and 24 ultrasonic group data. The two-tailed testing method (degree-of-freedom = 23) was used to assess a significant difference of the data with the software SPSS Statistics. The statistical results are given in Table S3. According to the statistical results, the value "*t*" is much greater than "1" ( $t \gg 1$ ) and the value "*P*" is less than "0.05" ( $P < 0.05$ ) at different depths (0–10  $\mu\text{m}$ ), indicating statistically significant differences between the heat group and ultrasonic group at different depths (0–10  $\mu\text{m}$ ). The data at depths of 15–30  $\mu\text{m}$  do not show a significant difference ( $P > 0.05$ ), where the brightness is close to the background brightness. A Student's *t* test was also applied to certify the validity of the experimental data in enhancing the skin moisture content. The quantitative values of the skin moisture content were selected as the

analysis objects. The total sample size "*n*" is 100, including 50 ultrasonic group data and 50 control group data. A two-tailed testing method (degree-of-freedom = 49) was used to assess significant difference of the data with the software SPSS Statistics. The statistical results are given in Table S4. According to the results, the value "*t*" is much greater than "1" ( $t \gg 1$ ) and the value "*P*" is less than "0.05" ( $P < 0.05$ ), which indicates that the data from the experiments of enhancing the skin moisture content are statistically significant.

**Human Dermal Fibroblast Culture.** The fibroblasts were cultured in DMEM containing 10% FBS, 1% antibiotic-antimycotic, and 1% L-glutamine at 37 °C and a 5% CO<sub>2</sub> humidified atmosphere. When the confluence of cells reached about 80%, adherent fibroblasts were trypsinized and passaged using 0.05% tryp-EDTA (GIBCO).

**Cell Cytotoxicity.** (1) Live/dead assay: The cell viability was detected by the live/dead kit (Yeasen, China). In brief, the cells were seeded into 24-well plates at a density of  $4 \times 10^4$  per mL. Then, the SEFM were added and cocultured with cells in a standard environment at 37 °C with 5% CO<sub>2</sub>. And then the fibroblasts were tested by the live/dead kit for 40 min at 37 °C according to the instruction (days 1, 3, and 5, respectively). After that, the fibroblasts were examined using a fluorescence microscope (Nikon, Japan). The living cells appeared as emerald green, and dead cells appeared as red. (2) CCK-8 assay: The cytotoxicities of SEFM on fibroblasts were investigated using CCK-8 (Beyotime, China) according to the instructions. Briefly, the cells were seeded into 24-well plates at a density of  $4 \times 10^4$  per milliliter. The cells were cocultured as the above-described protocol. The CCK-8 solution (20  $\mu\text{L}$ ) was added to each well on days 1, 3, and 5 of the experiment, respectively. The plate was incubated at 37 °C for 1 h in the dark, then the OD value of the solution was detected at 450 nm using a microplate reader.

**Additional Experimental Details.** The experiments involving human volunteers were approved by the Institutional Review Board at the Institute of Mechanics, Chinese Academy of Sciences (Approval No. 2021003), wherein the volunteers took part following informed consent. The animal experiments were also approved by the Institutional Review Board at Institute of Mechanics, Chinese Academy of Sciences (Approval No. 2021003).

## ASSOCIATED CONTENT

### Supporting Information

The Supporting Information is available free of charge at <https://pubs.acs.org/doi/10.1021/acsnano.1c11181>.

The visual effect that the SEFM emits ultrasound to a water drop (MP4)

The visual effect that the SEFM emits ultrasound to 3  $\times$  3 water drops (MP4)

Establishment process of the face-like silicone layer by FEA; calculation of the bending and tensile stiffnesses; theoretical modeling of one-dimensional piezoelectric vibrator; tensile test of the rectangular sample of the SEFM; material parameters in the FEA; geometric model and meshes in the FEA of sound field; simulated results of sound field; detailed statistical data; detailed layout of the island-bridge mesh circuit; details on the encapsulation process; robustness of the mechanical and electrical properties; more impedance–frequency curves; more confocal micrographs; experiment on thermal effect; delivery of beta-glucan and d-panthenol (PDF)

## AUTHOR INFORMATION

### Corresponding Author

Yewang Su – State Key Laboratory of Nonlinear Mechanics, Institute of Mechanics, Chinese Academy of Sciences, Beijing 100190, China; School of Engineering Science, University of Chinese Academy of Sciences, Beijing 100049, China; State

Key Laboratory of Acoustics, Institute of Acoustics, Chinese Academy of Sciences, Beijing 100190, China; [orcid.org/0000-0002-5961-0490](https://orcid.org/0000-0002-5961-0490); Email: [yewangsu@imech.ac.cn](mailto:yewangsu@imech.ac.cn)

## Authors

**Shuang Li** – State Key Laboratory of Nonlinear Mechanics, Institute of Mechanics, Chinese Academy of Sciences, Beijing 100190, China; School of Engineering Science, University of Chinese Academy of Sciences, Beijing 100049, China

**Jingwen Xu** – State Key Laboratory of Membrane Biology, Institute of Zoology, Chinese Academy of Sciences, Beijing 100101, China; University of Chinese Academy of Sciences, Beijing 100049, China

**Rui Li** – State Key Laboratory of Structural Analysis for Industrial Equipment, Department of Engineering Mechanics, and International Research Center for Computational Mechanics, Dalian University of Technology, Dalian 116024, China

**Yongkang Wang** – State Key Laboratory of Nonlinear Mechanics, Institute of Mechanics, Chinese Academy of Sciences, Beijing 100190, China; School of Engineering Science, University of Chinese Academy of Sciences, Beijing 100049, China

**Maoyi Zhang** – State Key Laboratory of Nonlinear Mechanics, Institute of Mechanics, Chinese Academy of Sciences, Beijing 100190, China; School of Engineering Science, University of Chinese Academy of Sciences, Beijing 100049, China

**Jie Li** – Institute for Advanced Ceramics, State Key Laboratory of Urban Water Resource and Environment, Harbin Institute of Technology, Harbin 150001, China

**Shizhen Yin** – State Key Laboratory of Nonlinear Mechanics, Institute of Mechanics, Chinese Academy of Sciences, Beijing 100190, China; School of Engineering Science, University of Chinese Academy of Sciences, Beijing 100049, China

**Guodong Liu** – State Key Laboratory of Nonlinear Mechanics, Institute of Mechanics, Chinese Academy of Sciences, Beijing 100190, China; School of Engineering Science, University of Chinese Academy of Sciences, Beijing 100049, China

**Lijuan Zhang** – State Key Laboratory of Nonlinear Mechanics, Institute of Mechanics, Chinese Academy of Sciences, Beijing 100190, China; School of Engineering Science, University of Chinese Academy of Sciences, Beijing 100049, China

**Baoqiang Li** – Institute for Advanced Ceramics, State Key Laboratory of Urban Water Resource and Environment, Harbin Institute of Technology, Harbin 150001, China; [orcid.org/0000-0003-0278-4542](https://orcid.org/0000-0003-0278-4542)

**Qi Gu** – State Key Laboratory of Membrane Biology, Institute of Zoology, Chinese Academy of Sciences, Beijing 100101, China; University of Chinese Academy of Sciences, Beijing 100049, China; Beijing Institute for Stem Cell and Regenerative Medicine, Beijing 100101, China; [orcid.org/0000-0001-9387-9525](https://orcid.org/0000-0001-9387-9525)

Complete contact information is available at: <https://pubs.acs.org/10.1021/acsnano.1c11181>

## Author Contributions

S.L. and Y.S. conceived the concept. S.L., J.X., R.L., Y.W., M.Z., J.L., S.Y., G.L., L.Z., B.L., Q.G., and Y.S. conducted the theoretical derivation, FEA, experimental fabrication, and performance test and discussed all of the data. S.L., R.L., and Y.S. prepared the manuscript. Y.S. supervised the project.

## Notes

The authors declare no competing financial interest.

## ACKNOWLEDGMENTS

Y.S. gratefully acknowledges the support from the National Natural Science Foundation of China (grants 12172359 and 11772331), Beijing Municipal Science and Technology Commission (Z191100002019010), Beijing Municipal Natural Science Foundation (No. 2202066), Key Research Program of Frontier Sciences of the Chinese Academy of Sciences (ZDBS-LY-JSC014), CAS Interdisciplinary Innovation Team (JCTD-2020-03), Strategic Priority Research Program of the Chinese Academy of Sciences (No. XDB22040501), and State Key Laboratory of Acoustics, Chinese Academy of Sciences (SKLA202109). R.L. gratefully acknowledges the support from the National Natural Science Foundation of China (grants 12022209 and 11972103), Liaoning Revitalization Talents Program (grant XLYC1807126), and the Fundamental Research Funds for the Central Universities (grant DUT21-LAB124). Q.G. gratefully acknowledges the support from the Strategic Priority Research Program of Chinese Academy of Sciences (No. XDA16020802), the Research Equipment Development Program of the Chinese Academy of Sciences (No. YJKYYQ20190045), Foundation of State Key Laboratory of Robotics (2017-Z16), and the financial support from the State Key Laboratory of Membrane and the State Key Laboratory of Robotics. We are also grateful to Shenglong Ding and Song Han for their outstanding technical support of the cell viability test and Yuqun Lan, Yang Zhao, Juyao Li, and Integrated System Ltd. (China) for the sound field measurement.

## REFERENCES

- (1) Prausnitz, M. R.; Langer, R. Transdermal Drug Delivery. *Nat. Biotechnol.* **2008**, *26*, 1261–1268.
- (2) Karande, P.; Jain, A.; Ergun, K.; Kispersky, V.; Mitragotri, S. Design Principles of Chemical Penetration Enhancers for Transdermal Drug Delivery. *Proc. Natl. Acad. Sci. U. S. A.* **2005**, *102*, 4688–4693.
- (3) Williams, A. C.; Barry, B. W. Penetration Enhancers. *Adv. Drug Deliver. Rev.* **2004**, *56*, 603–618.
- (4) Kalia, Y. N.; Naik, A.; Garrison, J.; Guy, R. H. Iontophoretic Drug Delivery. *Adv. Drug Deliver. Rev.* **2004**, *56*, 619–658.
- (5) Pikal, M. J. The Role of Electroosmotic Flow in Transdermal Iontophoresis. *Adv. Drug Deliver. Rev.* **1992**, *9*, 201–237.
- (6) Werman, R.; Davidoff, R. A.; Aprison, M. H. Inhibition of Motoneurons by Iontophoresis of Glycine. *Nature* **1967**, *214*, 681–683.
- (7) Pu, Z. H.; Zhang, X. G.; Yu, H. X.; Tu, J. A.; Chen, H. L.; Liu, Y. C.; Su, X.; Wang, R. D.; Zhang, L.; Li, D. C. A Thermal Activated and Differential Self-Calibrated Flexible Epidermal Biomicrofluidic Device for Wearable Accurate Blood Glucose Monitoring. *Sci. Adv.* **2021**, *7*, DOI: 10.1126/sciadv.abd0199.
- (8) Mitragotri, S. Innovation - Healing Sound: the Use of Ultrasound in Drug Delivery and Other Therapeutic Applications. *Nat. Rev. Drug Discovery* **2005**, *4*, 255–260.
- (9) Ueda, H.; Sugibayashi, K.; Morimoto, Y. Skin Penetration-Enhancing Effect of Drugs by Phonophoresis. *J. Controlled Release* **1995**, *37*, 291–297.
- (10) Amani, H.; Shahbazi, M. A.; D'Amico, C.; Fontana, F.; Abbaszadeh, S.; Santos, H. A. Microneedles for Painless Transdermal Immunotherapeutic Applications. *J. Controlled Release* **2021**, *330*, 185–217.
- (11) Sivamani, R. K.; Liepmann, D.; Maibach, H. I. Microneedles and Transdermal Applications. *Expert Opin. Drug Del.* **2007**, *4*, 19–25.
- (12) Yang, B.; Fang, X. E.; Kong, J. L. Engineered Microneedles for Interstitial Fluid Cell-Free DNA Capture and Sensing Using



Iontophoretic Dual-Extraction Wearable Patch. *Adv. Funct. Mater.* **2020**, *30*, 2000591.

(13) Park, S. R.; Jang, K. W.; Park, S. H.; Cho, H. S.; Jin, C. Z.; Choi, M. J.; Chung, S. I.; Min, B. H. The Effect of Sonication on Simulated Osteoarthritis. Part I: Effects of 1 MHz Ultrasound on Uptake of Hyaluronan into the Rabbit Synovium. *Ultrasound Med. Biol.* **2005**, *31*, 1551–1558.

(14) Yoon, J.; Park, D.; Son, T.; Seo, J.; Nelson, J. S.; Jung, B. A Physical Method to Enhance Transdermal Delivery of a Tissue Optical Clearing Agent: Combination of Microneedling and Sonophoresis. *Lasers Surg. Med.* **2010**, *42*, 412–417.

(15) Hakozaki, T.; Takiwaki, H.; Miyamoto, K.; Sato, Y.; Arase, S. Ultrasound Enhanced Skin-Lightening Effect of Vitamin C and Niacinamide. *Skin Res. Technol.* **2006**, *12*, 105–113.

(16) Lopez, R. F. V.; Seto, J. E.; Blankschtein, D.; Langer, R. Enhancing the Transdermal Delivery of Rigid Nanoparticles Using the Simultaneous Application of Ultrasound and Sodium Lauryl sulfate. *Biomaterials* **2011**, *32*, 933–941.

(17) Mitragotri, S. Sonophoresis: A 50-Year Journey. *Drug Discovery Today* **2004**, *9*, 735–736.

(18) Polat, B. E.; Hart, D.; Langer, R.; Blankschtein, D. Ultrasound-Mediated Transdermal Drug Delivery: Mechanisms, Scope, and Emerging Trends. *J. Controlled Release* **2011**, *152*, 330–348.

(19) Bommannan, D.; Menon, G. K.; Okuyama, H.; Elias, P. M.; Guy, R. H. Sonophoresis. 2. Examination of the Mechanism(S) of Ultrasound-Enhanced Transdermal Drug Delivery. *Pharm. Res.* **1992**, *9*, 1043–1047.

(20) Bommannan, D.; Okuyama, H.; Stauffer, P.; Guy, R. H. Sonophoresis. 1. The Use of High-Frequency Ultrasound to Enhance Transdermal Drug Delivery. *Pharm. Res.* **1992**, *9*, 559–564.

(21) Brucks, R.; Nanavaty, M.; Jung, D.; Siegel, F. The Effect of Ultrasound on the In Vitro Penetration of Ibuprofen through Human Epidermis. *Pharm. Res.* **1989**, *6*, 697–701.

(22) Levy, D.; Kost, J.; Meshulam, Y.; Langer, R. Effect of Ultrasound on Transdermal Drug Delivery to Rats and Guinea-Pigs. *J. Clin. Invest.* **1989**, *83*, 2074–2078.

(23) Mitragotri, S.; Blankschtein, D.; Langer, R. Ultrasound-Mediated Transdermal Protein Delivery. *Science* **1995**, *269*, 850–853.

(24) Matts, P. J.; Fink, B.; Grammer, K.; Burquest, M. Color Homogeneity and Visual Perception of Age, Health, and Attractiveness of Female Facial Skin. *J. Am. Acad. Dermatol.* **2007**, *57*, 977–984.

(25) Shackelford, T. K.; Larsen, R. J. Facial Attractiveness and Physical Health. *Evol. Hum. Behav.* **1999**, *20*, 71–76.

(26) Smithard, A.; Glazebrook, C.; Williams, H. C. Acne Prevalence, Knowledge about Acne and Psychological Morbidity in Mid-Adolescence: A Community-Based Study. *Br. J. Dermatol.* **2001**, *145*, 274–279.

(27) Azagury, A.; Khoury, L.; Enden, G.; Kost, J. Ultrasound Mediated Transdermal Drug Delivery. *Adv. Drug Deliver. Rev.* **2014**, *72*, 127–143.

(28) Polat, B. E.; Blankschtein, D.; Langer, R. Low-Frequency Sonophoresis: Application to the Transdermal Delivery of Macromolecules and Hydrophilic Drugs. *Expert Opin. Drug Del.* **2010**, *7*, 1415–1432.

(29) Hu, H.; Zhu, X.; Wang, C.; Zhang, L.; Li, X.; Lee, S.; Huang, Z.; Chen, R.; Chen, Z.; Wang, C.; Gu, Y.; Chen, Y.; Lei, Y.; Zhang, T.; Kim, N.; Guo, Y.; Teng, Y.; Zhou, W.; Li, Y.; Nomoto, A.; Sternini, S.; Zhou, Q.; Pharr, M.; di Scalea, F. L.; Xu, S. Stretchable Ultrasonic Transducer Arrays for Three-Dimensional Imaging on Complex Surfaces. *Sci. Adv.* **2018**, *4*, eaar3979.

(30) Kim, T.; Cui, Z.; Chang, W.-y.; Kim, H.; Zhu, Y.; Jiang, X. Flexible 1–3 Composite Ultrasound Transducers With Silver-Nanowire-Based Stretchable Electrodes. *IEEE T. Ind. Electron.* **2020**, *67*, 6955–6962.

(31) Liu, H.; Geng, J.; Zhu, Q.; Zhang, L.; Wang, F.; Chen, T.; Sun, L. Flexible Ultrasonic Transducer Array with Bulk PZT for Adjuvant Treatment of Bone Injury. *Sensors* **2020**, *20*, 86.

(32) Liu, T.; Dangi, A.; Kim, J. N.; Kothapalli, S.-r.; Choi, K.; Trolier-McKinstry, S.; Jackson, T. Flexible Thin-Film PZT Ultrasonic Transducers on Polyimide Substrates. *Sensors* **2021**, *21*, 1014.

(33) Liu, W.; Zhu, C.; Wu, D. Flexible Piezoelectric Micro Ultrasonic Transducer Array Integrated on Various Flexible Substrates. *Sensor. Actuat. A-Phys.* **2021**, *317*, 112476.

(34) Liu, W.; Zhu, C.; Wu, D. Flexible and Stretchable Ultrasonic Transducer Array Conformed to Complex Surfaces. *IEEE Electr. Device L.* **2021**, *42*, 240–243.

(35) Lyu, W.; Ma, Y.; Chen, S.; Li, H.; Wang, P.; Chen, Y.; Feng, X. Flexible Ultrasonic Patch for Accelerating Chronic Wound Healing. *Adv. Healthc. Mater.* **2021**, *10*, 2100785.

(36) Pashaei, V.; Dehghanzadeh, P.; Enwia, G.; Bayat, M.; Majerus, S. J. A.; Mandal, S. Flexible Body-Conformal Ultrasound Patches for Image-Guided Neuromodulation. *IEEE T. Biomed. Circ. S.* **2020**, *14*, 305–318.

(37) Peng, C.; Chen, M.; Sim, H. K.; Zhu, Y.; Jiang, X. Noninvasive and Nonocclusive Blood Pressure Monitoring via a Flexible Piezo-Composite Ultrasonic Sensor. *IEEE Sens. J.* **2021**, *21*, 2642–2650.

(38) Wang, C.; Li, X.; Hu, H.; Zhang, L.; Huang, Z.; Lin, M.; Zhang, Z.; Yin, Z.; Huang, B.; Gong, H.; Bhaskaran, S.; Gu, Y.; Makihata, M.; Guo, Y.; Lei, Y.; Chen, Y.; Wang, C.; Li, Y.; Zhang, T.; Chen, Z.; et al. Monitoring of the Central Blood Pressure Waveform via a Conformal Ultrasonic Device. *Nat. Biomed. Eng.* **2018**, *2*, 687–695.

(39) Wang, C.; Qi, B.; Lin, M.; Zhang, Z.; Makihata, M.; Liu, B.; Zhou, S.; Huang, Y.-h.; Hu, H.; Gu, Y.; Chen, Y.; Lei, Y.; Lee, T.; Chien, S.; Jang, K.-I.; Kistler, E. B.; Xu, S. Continuous Monitoring of Deep-Tissue Haemodynamics with Stretchable Ultrasonic Phased Arrays. *Nat. Biomed. Eng.* **2021**, *5*, 749–758.

(40) Wang, F.; Jin, P.; Feng, Y.; Fu, J.; Wang, P.; Liu, X.; Zhang, Y.; Ma, Y.; Yang, Y.; Yang, A.; Feng, X. Flexible Doppler Ultrasound Device for the Monitoring of Blood Flow Velocity. *Sci. Adv.* **2021**, *7*, eabi9283.

(41) Wang, Z.; Xue, Q.-t.; Chen, Y.-q.; Shu, Y.; Tian, H.; Yang, Y.; Xie, D.; Luo, J.-w.; Ren, T.-l. A Flexible Ultrasound Transducer Array with Micro-Machined Bulk PZT. *Sensors* **2015**, *15*, 2538–2547.

(42) Xue, Y.; Zhou, C.; Zhang, X. Y.; Chan, M. A Flexible High Quality-Factor Bulk Acoustic Resonator Enabled with Transferred Single-Crystal Piezoelectric Thin Film for Sensing Applications. *Sensor. Actuat. A-Phys.* **2021**, *326*, 112721.

(43) Yokus, M. A.; Daniele, M. A. Integrated Non-Invasive Biochemical and Biophysical Sensing Systems for Health and Performance Monitoring: A Systems Perspective. *Biosens. Bioelectron.* **2021**, *184*, 113249.

(44) AlMohimeed, I.; Ono, Y. Flexible and Wearable Ultrasonic Sensor for Assessment of Skeletal Muscle Contractile Properties. In *2019 IEEE International Conference on Flexible and Printable Sensors and Systems (FLEPS)*; Glasgow, UK, July 8–10, 2019; IEEE: Glasgow, UK, 2019; pp 1–3.

(45) Li, R.; Li, M.; Su, Y. W.; Song, J. Z.; Ni, X. Q. An Analytical Mechanics Model for the Island-Bridge Structure of Stretchable Electronics. *Soft Matter* **2013**, *9*, 8476–8482.

(46) Su, Y. W.; Wu, J.; Fan, Z. C.; Hwang, K. C.; Song, J. Z.; Huang, Y. G.; Rogers, J. A. Postbuckling Analysis and Its Application to Stretchable Electronics. *J. Mech. Phys. Solids* **2012**, *60*, 487–508.

(47) Xu, S.; Zhang, Y.; Cho, J.; Lee, J.; Huang, X.; Jia, L.; Fan, J. A.; Su, Y.; Su, J.; Zhang, H.; Cheng, H.; Lu, B.; Yu, C.; Chuang, C.; Kim, T.-i.; Song, T.; Shigeta, K.; Kang, S.; Dagdeviren, C.; Petrov, I.; Braun, P. V.; Huang, Y.; Paik, U.; Rogers, J. A. Stretchable Batteries with Self-Similar Serpentine Interconnects and Integrated Wireless Recharging Systems. *Nat. Commun.* **2013**, *4*, 1543.

(48) Han, M. D.; Chen, L.; Aras, K.; Liang, C. M.; Chen, X. X.; Zhao, H. B.; Li, K.; Faye, N. R.; Sun, B. H.; Kim, J. H.; Bai, W. B.; Yang, Q. S.; Ma, Y. H.; Lu, W.; Song, E. M.; Baek, J. M.; Lee, Y. J.; Liu, C.; Model, J. B.; Yang, G. J.; et al. Catheter-Integrated Soft Multilayer Electronic Arrays for Multiplexed Sensing and Actuation During Cardiac Surgery. *Nat. Biomed. Eng.* **2020**, *4*, 997–1009.

(49) Su, Y. W.; Ping, X. C.; Yu, K. J.; Lee, J. W.; Fan, J. A.; Wang, B.; Li, M.; Li, R.; Harburg, D. V.; Huang, Y. A.; Yu, C. J.; Mao, S. M.;



Shim, J.; Yang, Q. L.; Lee, P. Y.; Armonas, A.; Choi, K. J.; Yang, Y. C.; Paik, U.; Chang, T.; et al. In-Plane Deformation Mechanics for Highly Stretchable Electronics. *Adv. Mater.* **2017**, *29*, 1604989.

(50) Lu, N. S.; Suo, Z. G.; Vlassak, J. J. The Effect of Film Thickness on the Failure Strain of Polymer-Supported Metal Films. *Acta Mater.* **2010**, *58*, 1679–1687.

(51) Lu, N. S.; Wang, X.; Suo, Z. G.; Vlassak, J. Metal Films on Polymer Substrates Stretched Beyond 50%. *Appl. Phys. Lett.* **2007**, *91*, 221909.

(52) Zhang, L. J.; Jiang, X. X.; Jiang, W.; Li, S.; Chi, Y. X.; Liu, H.; Zhang, M. Y.; Li, J. Y.; Fang, M.; Pan, B.; Chen, Y. L.; Shen, C. N.; Guo, X.; Li, R.; Guo, L.; Su, Y. W. Infrared Skin-Like Active Stretchable Electronics Based on Organic-Inorganic Composite Structures for Promotion of Cutaneous Wound Healing. *Adv. Mater. Technol.* **2019**, *4*, 1900150.

(53) Cheng, X.; Zhang, F.; Bo, R. H.; Shen, Z. M.; Pang, W. B.; Jin, T. Q.; Song, H. L.; Xue, Z. G.; Zhang, Y. H. An Anti-Fatigue Design Strategy for 3D Ribbon-Shaped Flexible Electronics. *Adv. Mater.* **2021**, *33*, 2102684.

(54) Ko, H. C.; Stoykovich, M. P.; Song, J. Z.; Malyarchuk, V.; Choi, W. M.; Yu, C. J.; Geddes, J. B.; Xiao, J. L.; Wang, S. D.; Huang, Y. G.; Rogers, J. A. A Hemispherical Electronic Eye Camera Based on Compressible Silicon Optoelectronics. *Nature* **2008**, *454*, 748–753.

(55) Gao, Q.; Kopera, B. A. F.; Zhu, J.; Liao, X. J.; Gao, C.; Retsch, M.; Agarwal, S.; Greiner, A. Breathable and Flexible Polymer Membranes with Mechanoresponsive Electric Resistance. *Adv. Funct. Mater.* **2020**, *30*, 1907555.

(56) Gong, M.; Wan, P. B.; Ma, D.; Zhong, M. J.; Liao, M. H.; Ye, J. J.; Shi, R.; Zhang, L. Q. Flexible Breathable Nanomesh Electronic Devices for On-Demand Therapy. *Adv. Funct. Mater.* **2019**, *29*, 1902127.

(57) Gerratt, A. P.; Michaud, H. O.; Lacour, S. P. Elastomeric Electronic Skin for Prosthetic Tactile Sensation. *Adv. Funct. Mater.* **2015**, *25*, 2287–2295.

(58) Kaneko, A.; Asai, N.; Kanda, T. The Influence of Age on Pressure Perception of Static and Moving Two-Point Discrimination in Normal Subjects. *J. Hand Ther.* **2005**, *18*, 421–425.

(59) Kim, D. H.; Lu, N. S.; Ma, R.; Kim, Y. S.; Kim, R. H.; Wang, S. D.; Wu, J.; Won, S. M.; Tao, H.; Islam, A.; Yu, K. J.; Kim, T. I.; Chowdhury, R.; Ying, M.; Xu, L. Z.; Li, M.; Chung, H. J.; Keum, H.; McCormick, M.; Liu, P.; et al. Epidermal Electronics. *Science* **2011**, *333*, 838–843.

(60) Rosenbaum, J. F. *Bulk Acoustic Wave Theory and Devices*; Artech House: Boston, 1988.

(61) Zhou, H. Y.; Huang, S. H.; Li, W. Electrical Impedance Matching Between Piezoelectric Transducer and Power Amplifier. *IEEE Sens. J.* **2020**, *20*, 14273–14281.

(62) Vyklicky, L.; Vlachova, V.; Vitaskova, Z.; Dittert, I.; Kabat, M.; Orkand, R. K. Temperature Coefficient of Membrane Currents Induced by Noxious Heat in Sensory Neurones in the Rat. *J. Physiol-London* **1999**, *517*, 181–192.

(63) Juncan, A. M.; Moisa, D. G.; Santini, A.; Morgovan, C.; Rus, L. L.; Vonica-Tincu, A. L.; Loghin, F. Advantages of Hyaluronic Acid and Its Combination with Other Bioactive Ingredients in Cosmeceuticals. *Molecules* **2021**, *26*, 4429.

(64) Toole, B. P. Hyaluronan: From Extracellular Glue to Pericellular Cue. *Nat. Rev. Cancer* **2004**, *4*, 528–539.

(65) Wang, H. L.; Fan, P. F.; Guo, X. S.; Tu, J.; Ma, Y.; Zhang, D. Ultrasound-Mediated Transdermal Drug Delivery of Fluorescent Nanoparticles and Hyaluronic Acid into Porcine Skin in Vitro. *Chinese Phys. B* **2016**, *25*, 124314.

(66) Du, B.; Bian, Z. X.; Xu, B. J. Skin Health Promotion Effects of Natural Beta-Glucan Derived from Cereals and Microorganisms: A Review. *Phytother. Res.* **2014**, *28*, 159–166.

(67) Wang, L. H.; Tseng, S. W. Direct Determination of D-Panthenol and Aalt of Pantothenic Acid in Cosmetic and Pharmaceutical Preparations by Differential Pulse Voltammetry. *Anal. Chim. Acta* **2001**, *432*, 39–48.

## Recommended by ACS

### Skin-Like Near-Infrared II Photodetector with High Performance for Optical Communication, Imaging, and Proximity Sensing

Yu Zhu, Yongsheng Chen, *et al.*

FEBRUARY 23, 2023  
CHEMISTRY OF MATERIALS

READ 

### Tissue Clearing and Its Application in the Musculoskeletal System

Yan-Jing Zhan, Nan Jiang, *et al.*

JANUARY 05, 2023  
ACS OMEGA

READ 

### Palette of Rechargeable Mechanoluminescent Fluids Produced by a Biomineral-Inspired Suppressed Dissolution Approach

Fan Yang, Guosong Hong, *et al.*

OCTOBER 03, 2022  
JOURNAL OF THE AMERICAN CHEMICAL SOCIETY

READ 

### Stretchable and Directly Patternable Double-Layer Structure Electrodes with Complete Coverage

Junsung Bang, Soong Ju Oh, *et al.*

AUGUST 04, 2022  
ACS NANO

READ 

Get More Suggestions >